Observation of Weyl and Dirac fermions at smooth topological Volkov-Pankratov heterojunctions

J. Bermejo-Ortiz,[1] G. Krizman ⬚,[2,*] R. Jakiela ⬚,[3] Z. Khosravizadeh ⬚,[3] M. Hajlaoui,[2] G. Bauer,[2] G. Springholz ⬚,[2] L.-A. de Vaulchier,[1] and Y. Guldner[1]

[1]*Laboratoire de Physique de l'Ecole normale supérieure, ENS, Université PSL, CNRS, Sorbonne Université, 24 rue Lhomond, 75005 Paris, France*
[2]*Institut für Halbleiter und Festkörperphysik, Johannes Kepler Universität, Altenbergerstrasse 69, 4040 Linz, Austria*
[3]*Institute of Physics, Polish Academy of Sciences, Warsaw, Poland*

Weyl and Dirac relativistic fermions are ubiquitous in topological matter. Their relativistic character enables high-energy physics phenomena like the chiral anomaly to occur in the solid state, which allows us to experimentally probe and explore fundamental relativistic theories. Here, we show that, on smooth interfaces between a trivial and a topological material, massless Weyl and massive Dirac fermions intrinsically coexist. The emergence of the latter, known as Volkov-Pankratov states, is directly revealed by magneto-optical spectroscopy, evidencing that their energy spectra are perfectly controlled by the smoothness of the topological interface. Simultaneously, we reveal the optical absorption of the zero-energy chiral Weyl state, whose wave function is drastically transformed when the topological interface is smooth. Artificial engineering of the topology profile thus provides a textbook system to explore the rich relativistic energy spectra in condensed matter heterostructures.

I. INTRODUCTION

Weyl and Dirac electrons have attracted tremendous interest, as they mimic relativistic high-energy particles. The properties of these electrons are governed by physical laws that resemble relativistic equations [1–3], and as a result, condensed matter and relativistic physics have emerged as tightly related fields. A striking example is the discovery of topological insulators (TIs), which are insulating in the bulk but exhibit a metallic chiral state (CS) at their boundaries [4–6]. These massless states obey the Weyl equation [1,7,8] and display a relativistic energy-momentum relation. As such, they are a hallmark of relativistic physics inherent to topological matter, and with the advent of topological systems, they have been coined *topological interface states*. They display a distinct chirality with the electron spin locked to its momentum protected by time-reversal or crystalline symmetry. This led to the discovery of phenomena such as the quantum spin Hall (QSH) [9,10] and quantum anomalous Hall effects [11,12] and opened the door for physics and device applications.

The fundamental origin of the topological interface state is the change of band topology an electron experiences at the boundary between a normal insulator (NI) and a TI. The generic system to showcase the topological interface state existence is thus a topological heterojunction (THJ), that is, a single NI/TI interface—gradual or abrupt—where a crossover of topology from a material with positive to one with negative, i.e., inverted band gap, occurs. Dictated by the fundamental

bulk-boundary correspondence principle that two topologically distinct regions cannot be connected or transformed from one to another without a band crossing at the interface, this intrinsically leads to the formation of a gapless interface state. In the most general terms, the topological crossover at a THJ can be widely extended in space and can consist of an arbitrarily varying band gap profile, if a distinct change of a certain topology invariant takes place. For this very reason, topological CSs emerge independently of how the band inversion evolves across the interface region. Although this fundamental prediction was disclosed by Volkov and Pankratov [7] and Pankratov *et al.* [8] almost 40 years ago, it has not been tested or proven by experiments. This is, on the one hand, due to the considerable technological challenge of fabricating gradual THJs with artificially varying band gap profiles produced on demand by band gap engineering; on the other hand, unlike the topological states formed at TI surfaces, the chiral interface state of a gradual THJ resides in a region enclosed by a NI and a TI material and, as such, is not accessible by the usual surface-sensitive probes like angle-resolved photoemission spectroscopy (ARPES) or scanning tunneling microscopy.

In this paper, we employ band structure engineering and molecular beam epitaxy (MBE) to create artificial THJs with perfectly controlled smooth band gap profiles, crossing zero along the junction direction. Probing the relativistic energy spectrum by magneto-optical spectroscopy, we show that the topological CS forms a perfectly robust zero-energy mode that is completely independent of the smoothness of the THJ transition. The chiral zero-energy mode persists for THJs as wide as 200 nm, which impressively validates the fundamental prediction of topologic band theory [4,7,13]. Our artificial

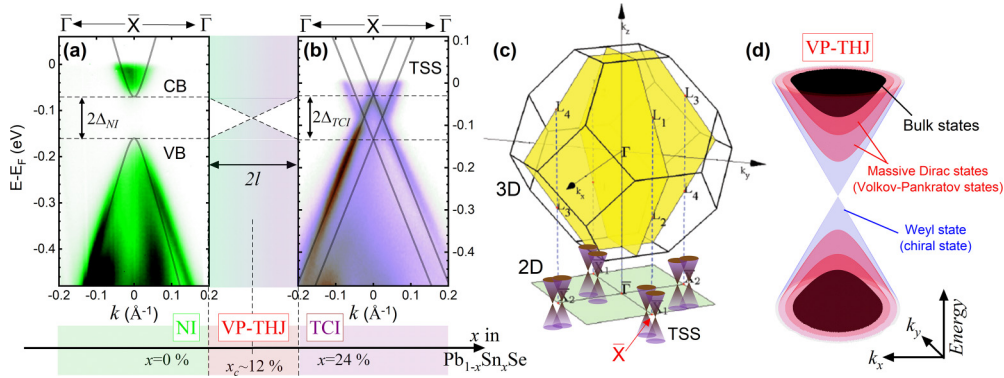*Corresponding author: gauthier.krizman@jku.at

FIG. 1. Smooth topological heterojunction (THJ) with the $Pb_{1-x}Sn_xSe$ system. Energy-momentum spectra of (a) normal insulator (NI) PbSe and (b) topological crystalline insulator (TCI) $Pb_{0.76}Sn_{0.24}Se$ measured by angle-resolved photoemission spectroscopy (ARPES) at $T = 10$ K, at the surface of epitaxial layers grown on (001) KCl substrates. Note that the samples were intentionally highly *n*-doped to shift the Fermi energy deep into the conduction band. The analysis yields a band gap of $2\Delta_{NI} = +90$ meV and $2\Delta_{TCI} = -95$ meV for (a) and (b), respectively (dashed lines), evidencing the band inversion. The solid lines in (a) represent the $E(k)$ dispersions of the PbSe bulk bands and in (b) the Dirac cones of the TSS of $Pb_{0.76}Sn_{0.24}Se$ as derived by $\mathbf{k} \cdot \mathbf{p}$ theory. By grading of composition x, the band gap can be smoothly tuned from positive to negative to form Volkov-Pankratov THJs (VP-THJs) with well-defined widths $2l$, as illustrated between (a) and (b). (c) Bulk and (001)-surface Brillouin zones of $Pb_{1-x}Sn_xSe$. In the bulk, the band inversions occur at the L points, which are projected pairwise to the $\bar{X}$ points (red dots) on the (001) surface. The coupling within each pair splits the TSS into a double Dirac cone due to the Lifshitz transition as seen in (b). (d) Typical two-dimensional (2D) energy spectrum of a sufficiently smooth VP-THJ, where massless Weyl (blue) and massive Dirac (red) fermions are located energetically within the bulk gap.

THJs are created using the lead tin chalcogenide $Pb_{1-x}Sn_xSe$ system in which the fundamental band gap 2Δ smoothly evolves from a positive to a negative value as the Sn concentration increases beyond a certain critical value x_c [14–16]. Accordingly, below x_c, the material is a NI, whereas above x_c, a topological crystalline insulator (TCI) with inverted band gap forms as signified by the appearance of a gapless topological surface state (TSS), as shown by Figs. 1(a)–1(c). By digital control of the alloy composition, we create smooth Volkov-Pankratov (VP) THJs with arbitrary junction widths to engineer on demand the transition $2\Delta(z)$ from the NI to the TCI state.

Probing the confined two-dimensional (2D) states of smooth THJs reveals the emergence of a relativistic energy spectrum that features massive Dirac fermions coexisting with a massless Weyl (the CS) fermion at a single interface, as illustrated by Fig. 1(d). While any THJ always supports one massless CS with definite chirality, here, we show that the additional massive states emerge only when the THJs become sufficiently wide. Following the prediction of the VP theory [7,8], these states are called VP states (VPSs) [7,8,17–19]. Like the CS, the VPSs are also chiral in nature and intrinsically relativistic but display a massive Dirac energy-momentum dispersion relation. The VPSs display a natural electron-hole symmetry, and although they are gapped, they lie within the band gaps of the confining TCI and NI regions. Moreover, their wave functions deeply extend into topological trivial and nontrivial regions, and as such, they fundamentally differ from classical confined 2D states in normal semiconductor heterojunctions, which encode, by a certain quantization, only the NI bulk band dispersions. By our experiments, we determine the critical value of the THJ width for the appearance of the VPSs and reveal that, thereafter, the number of VPSs increases, meaning that, contrary to the CS, multiple VPSs can be supported in a VP-THJ. We

particularly highlight the unique scaling properties of the VPS dependence on the junction width shown to be in perfect quantitative agreement with the VP theory [7,17]. Our VP-THJs thus represent a textbook system in which relativistic Weyl and Dirac fermions can be engineered in coexistence, which opens avenues for physics and device applications.

II. DESIGN AND FABRICATION OF VP-THJs

The formation of Weyl and Dirac fermions in gradual THJs demands a material system that allows a precise engineering of the band topology profile across the junction region. In this paper, we employ the lead tin chalcogenide system, specifically THJs based on $Pb_{1-x}Sn_xSe$ as envisioned in the VP work [7]. These belong to the IV-VI TCI class of materials [18–22] that features a smooth band inversion from NI to TCI when the Sn content increases [14] and, for this reason, is perfectly suited for topological band gap engineering. The IV-VI semiconductors have been extensively used for fabrication of quantum confined structures such as quantum wells [23–26] and quantum dots [27,28] used for a wide range of optoelectronic devices such as midinfrared laser diodes [29,30], vertical cavity surface emitting lasers [31], as well as focal plane arrays [25]. Moreover, carrier mobilities as high as $100\,000$ cm^2/Vsec can be reached in $Pb_{1-x}Sn_xSe$ [32], and the material can be made *n* or *p* type by impurity doping. Furthermore, IV-VI TCIs can support various topological phenomena such as Weyl nodes with ferroelectric distortions [33,34] or magnetic doping [35], one-dimensional (1D) step-edge states [36,37], as well as the QSH effect [38,39].

The $Pb_{1-x}Sn_xSe$ band structure is characterized by nearly mirror-symmetric conduction and valence bands with the band gaps located at the L points of the Brillouin zone (BZ) [40,41] [cf. Fig. 1(c)]. In the vicinity of these points, the conduction and valence bands are well described by $\mathbf{k} \cdot \mathbf{p}$

theory [40–42], and in good approximation, the fundamental band gap 2Δ linearly changes with Sn concentration x_{Sn} according to

$$2\Delta = 2\Delta_0(T, \varepsilon) - \alpha \cdot x_{Sn}, \tag{1}$$

where $\alpha \sim 800$ meV [14,16,43], and Δ_0 is the band gap of PbSe at a given temperature T and strain state ε that can be controlled by the epitaxial growth conditions. Accordingly, Δ changes from positive to negative at a critical Sn concentration $x_c = 2\Delta_0/\alpha$, at which the topological phase transition from the NI to the TCI state takes place. This is illustrated by Figs. 1(a) and 1(b), where energy-momentum maps of n-doped PbSe and $Pb_{0.76}Sn_{0.24}Se$ on KCl (001) substrates recorded by ARPES around the $\bar{X}$ point of the (001) surface BZ are depicted. Evidently, the band gap of NI PbSe is open, while that of the topological surface of $Pb_{0.76}Sn_{0.24}Se$ is closed, which directly evidences the nontrivial band topology and band inversion in this case.

For PbSe, the conduction and valence bands are in perfect agreement with $\mathbf{k} \cdot \mathbf{p}$ theory [26,38,40,41] represented by the solid lines in Fig. 1(a). Note that other energy bands lie $\sim$ 2 eV above and below the neutral point [15]. Therefore, the 2-band $\mathbf{k} \cdot \mathbf{p}$ Hamiltonian is almost unperturbed, which renders $Pb_{1-x}Sn_xSe$ a nearly perfect Dirac material like graphene. For the TCI $Pb_{0.76}Sn_{0.24}Se$, two Dirac cones appear at the surface [16,44] due to the pairwise projections of the symmetry inversions at the L points of the bulk three-dimensional (3D) BZ to the $\bar{X}$ points of the (001) surface BZ, as shown in Fig. 1(c). This leads to a splitting of the Dirac cones by the Lifshitz transition [16,45,46]. The inverted bulk band gap of $Pb_{0.76}Sn_{0.24}Se$ is given by the separation of the Lifshitz points at $\bar{X}$ ($k_\| = 0$) [16,45,46] where the two Dirac cones cross each other, as is indicated by the solid lines in Fig. 1(b). This yields the band gaps of PbSe and $Pb_{0.76}Sn_{0.24}Se$ as $2\Delta_{NI} = +90 \pm 10$ meV and $2\Delta_{TCI} = -95 \pm 10$ meV epilayers at 10 K. Note that, due to the epitaxial strain induced by the KCl substrate, these values differ from the bulk values [14,47]—the details of this will be reported elsewhere. Interpolation between these band gap values yields a critical Sn concentration $x_c \sim 12\%$ [see Eq. (1)] at which the band inversion takes place in our epilayers. By gradually increasing the Sn content from 0 to 0.24 during MBE growth, we can thus produce perfectly symmetric VP-THJs with the band inversion point located exactly in the middle of junction, as shown schematically in Figs. 1(a) and 1(b).

To create the graded $PbSe/Pb_{1-x}Sn_xSe$ THJ with well-controlled compositional profiles in the junction region, we employ MBE of digitally controlled ultrashort-period $PbSe/Pb_{0.76}Sn_{0.24}$ superlattices (SLs) in which the thickness ratio, and thus the SL composition, was incrementally changed over the junction region. This allows us to produce textbooklike THJs on demand with artificially engineered band profiles and topological transitions spanning between regions of large inverted/noninverted band gaps ($\sim \pm 95$ meV). The growth starts with a 200-nm-thick NI PbSe buffer layer on a (001) KCl substrate, followed by the digitally graded $Pb_{1-x}Sn_xSe$ junction region with linearly increasing Sn content from $x_{Sn} = 0$–24% in fine steps, as is ensured by the large number of up to 120 ultrathin layers in the junction region, as detailed in Appendix A. All THJs are terminated by a 200-nm
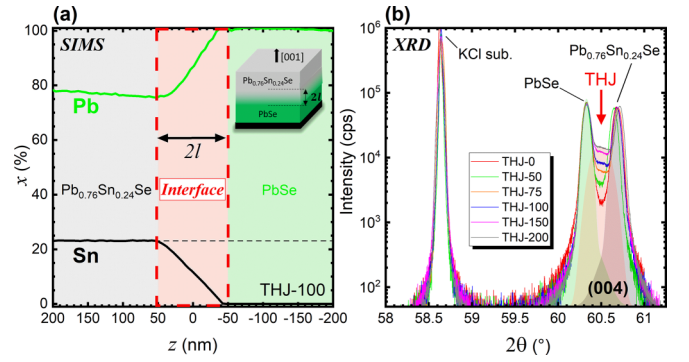

FIG. 2. Structural characterization of the Volkov-Pankratov topological heterojunction (VP-THJ). (a) Secondary ion-mass spectroscopy (SIMS) depth profile of the composition for the $PbSe/Pb_{0.76}Sn_{0.24}Se$ THJ-100 measured along the [001] growth direction, evidencing the linear change of the Pb and Sn concentration over the graded interface region. (b) X-ray diffraction spectra (using Cu $K\alpha 1$ radiation) around the (004) Bragg peak of the six investigated THJs with $2l$ varying from 0 up to 200 nm. The peaks from the KCl substrate, PbSe, and $Pb_{0.76}Sn_{0.24}Se$ are indicated. The diffraction curves are normalized to the PbSe peak.

$Pb_{0.76}Sn_{0.24}Se$ TCI layer with constant composition. A whole series of THJs with varying thicknesses $2l$ of the graded junction region was prepared, starting from $2l = 0$ (abrupt THJ) to $2l = 200$ nm, which is the widest THJ investigated in this paper. For clarity, the samples are labeled THJ-$2l$, where $2l$ corresponds to the thickness (in nm) of the smoothly graded interface layer.

The compositional profiles of the THJs were determined by secondary ion-mass spectroscopy (SIMS) [48]. Figure 2(a) shows the measured depth profiles of the Pb and Sn atom concentrations for the THJ with a 100-nm-wide junction region (THJ-100). As one can see, indeed the grading is essentially linear, and the total thickness of the junction region perfectly agrees with the targeted value. The sample structure was further analyzed by high-resolution x-ray diffraction, as shown in Fig. 2(b). For the graded THJ, the diffraction spectra feature two main peaks stemming from the 200-nm-thick bottom PbSe and top $Pb_{0.76}Sn_{0.24}Se$ layers with constant composition. The graded junction region shows up as a wide and almost constant intensity distribution in between these peaks [red shading in Fig. 2(b)] that is due to the continuously changing out-of-plane lattice parameter in the graded region that decreases from the value $a = 6.130$ Å of PbSe to 6.100 Å for $Pb_{0.76}Sn_{0.24}Se$. Evidently, its intensity rises proportionally to the thickness of the graded junction region [cf. Fig. 2(b)] and is thus a direct measure of the THJ width. Using Vegard's law [32] to determine the composition of the boundary layers of the THJ, we again find an excellent agreement with the targeted values, which proves the excellent control and reproducibility of our growth.

Using magneto-optical spectroscopy, we accurately determined the band gaps of the NI and TCI ends of the THJ (see Appendix B), giving $2\Delta_{NI} = 2\Delta(z < -l) = +95$ meV for the bottom PbSe and $2\Delta_{TCI} = 2\Delta(z > +l) = -95$ meV for the top $Pb_{0.76}Sn_{0.24}Se$ end of the VP-THJs, in perfect agreement with our ARPES measurement [Figs. 1(a) and 1(b)]. The

$2l$ width of the graded THJ region defines the slope of the band gap profile $\partial 2\Delta/\partial z = 2(\Delta_{NI} - \Delta_{TCI})/l$, giving a value of 1–10 meV/nm for the THJs with $2l = 20$–200 nm, respectively. The resulting THJ band gap profile is illustrated by Fig. 3(a) for the 100-nm junction width, indicating that, due to the symmetric structure, the topological transition $2\Delta(z) = 0$ is in the middle of the structure. The designed gap function $\Delta(z)$ was used as the input parameter for calculation of the relativistic eigenstates of the THJ using $\mathbf{k} \cdot \mathbf{p}$ theory described in Appendix C. The results are shown in the top panel of Fig. 3(a) for THJ-100 by the $E(k)$ dispersion curves of the bulk and topological interface state for the three NI, THJ, and TCI regions.

As shown in the middle panel of Fig. 3(a), for a smooth THJ, a series of confined interface states with clearly defined chirality $\alpha = \pm 1$ is predicted. These states consist of the gapless chiral Weyl state (CS) with zero mass and perfectly linear $E(k)$ dispersion as well as the additional VPSs that are gapped and display a finite mass [1,7,8,14–16]. According to our calculations, for a linearly graded THJ, they emerge exclusively under the conditions that the junction width $2l$ exceeds a critical value that is proportional to the characteristic length $\bar{\lambda} \sim \hbar \bar{v}_z/\bar{\Delta}$, defined by the averaged Dirac velocities $\bar{v}_z$ and band gaps $\bar{\Delta} > 0$ of the two endings of the THJ region. In fact, the number of VPSs is given by $l/2\bar{\lambda}$, as shown in detail below. A particularly interesting point is that the THJ grading strongly affects the wave function envelope of the CS, as illustrated in Fig. 3(b). Although its maximum is always at the band crossing point, for an abrupt interface, the CS wave function is cusped and rapidly decays exponentially on each side of the junction with a decay length $\bar{\lambda}/2$. On the contrary, for a gradual THJ, the CS wave function assumes the form of a Gaussian [see Fig. 3(b)] with a full width at half maximum proportional to $\sqrt{\bar{\lambda}l}$. Thus, the CS extends over a much wider region of space in a VP-THJ [17].

III. MAGNETO-OPTICAL SPECTROSCOPY OF THE WEYL AND DIRAC STATES

Having set the stage to study the relativistic spectrum of VP-THJs, we now turn to magneto-optical spectroscopy to detect the CS and VPS properties for different interface thicknesses. Figure 4(a) shows the magneto-optical spectra of the samples THJ-0, THJ-50, THJ-75, THJ-100, THJ-150, and THJ-200 measured at $T = 4.2$ K and magnetic field $B = 15$ T. In each case, we clearly observe distinct absorptions [blue and red arrows in Fig. 4(a)] at energies below the bulk band gaps $2|\Delta_{NI,TCI}| \approx 100$ meV. Strikingly, the lowest energy absorption, marked in blue, shows up at the same position for all THJs independent of their interface width, whereas the higher energy absorptions, marked in red, shift to lower energies when the heterojunction width $2l$ increases. This is a first clear indication that these absorptions arise from the VPS.

To quantitatively analyze the data, let us model the gradual interface using a half-gap function $\Delta(z)$ that smoothly changes along $z//[001]$. Using the theory developed by Volkov and Pankratov [7], Pankratov *et al.* [8], and by Lu and Goerbig [17], we express the Dirac Hamiltonian describing $Pb_{1-x}Sn_xSe$ alloys in the Weyl basis. Then the Hamiltonian of the gradual interface is derived and gives the following
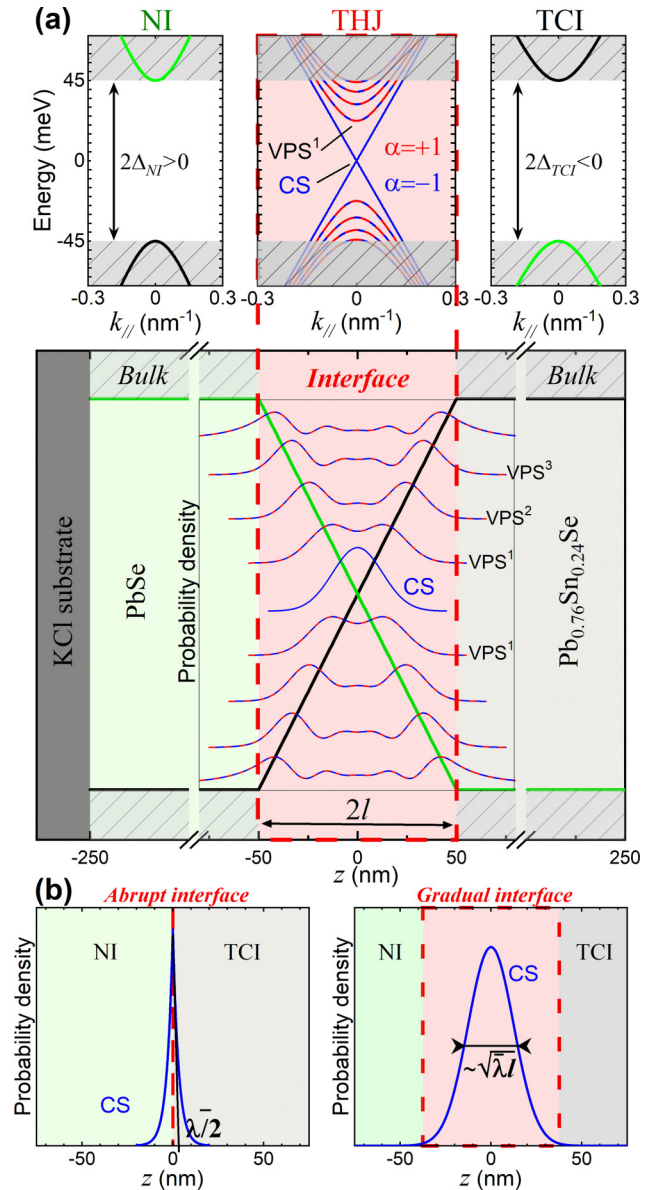

FIG. 3. Weyl and Volkov-Pankratov states (VPSs) formed in a smooth topological heterojunction (THJ). The THJ is illustrated for the case of a normal insulator (NI)/topological crystalline insulator (TCI) junction, consisting of NI PbSe on the one side and band-inverted TCI $Pb_{0.76}Sn_{0.24}Se$ on the other side that are connected by a 100-nm-thick linearly graded topological junction region where the Sn content increases from 0 to 24% (THJ-100 sample). (a) Top: Band diagrams (in-plane dispersions in the reciprocal space) for the three regions NI, THJ region, and TCI from left to right. The dispersions of the interface states are derived within a chiral basis $\alpha = \pm 1$ in red or blue. Middle: Real-space band edge profile along the $z//[001]$ direction illustrating the smooth inversion of the conduction and valence bands (green and black lines, respectively). Superimposed are the calculated square envelope wave functions of the massless chiral state (CS) and massive VPSs in the chiral basis. (b) Comparison of the envelope wave functions of the CS for the case of an abrupt (left) and a gradual (right) interface. For the abrupt interface, the black line denotes the tangent at $z = 0$, which defines the characteristic length $\bar{\lambda}/2$. For the gradual interface, the CS wave function has a Gaussian shape with a full width at half maximum (FWHM) given exactly by $2\sqrt{2\ln 2}\sqrt{\bar{\lambda}l}$.
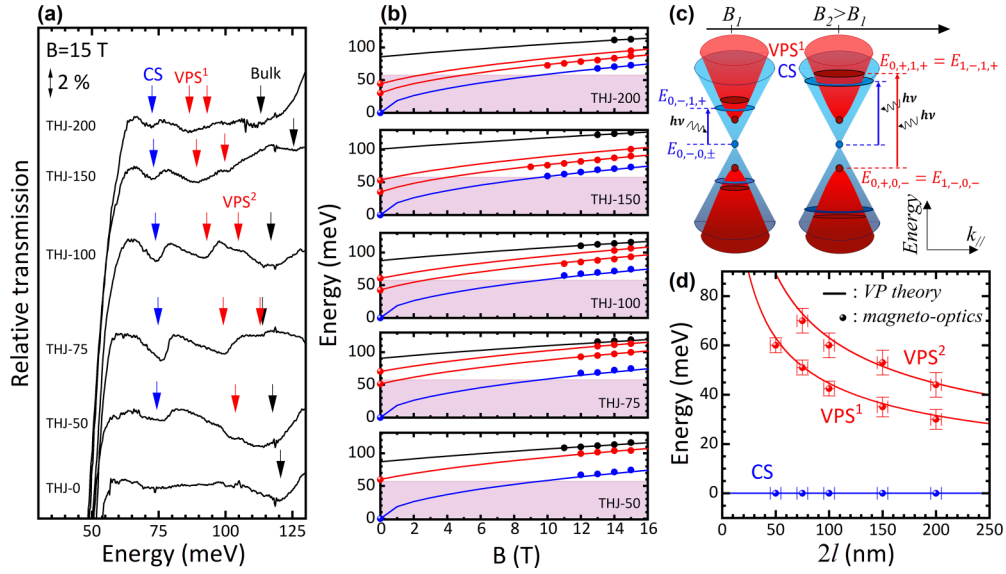
FIG. 4. Magneto-optical evidence of the Volkov-Pankratov topological heterojunction (VP-THJ) energy spectra. (a) Normalized transmission spectra at $B = 15$ T and $T = 4.2$ K for the six THJs with different widths varying from $2l = 0$ to 200 nm. The low-energy absorptions marked by blue, red, and black arrows denote the optical transitions involving the chiral state (CS), Volkov-Pankratov state (VPS), and bulk, respectively. A 2% absorption scale bar is shown. (b) Landau level fan charts of the absorptions (dots) plotted together with the fit of the ground transitions using Eq. (4). Blue is for the CS; VPS^1 and VPS^2 are in red; and the ground interband transitions of bulk $Pb_{0.76}Sn_{0.24}Se$ are plotted in black. The shaded purple region indicates the experimentally inaccessible energy range. (c) Quantized band structure of CS and VPS^1 in a perpendicular magnetic field, shown for two arbitrary magnetic fields B_1 and B_2. The Weyl and Dirac cones are quantized in terms of Landau levels with energies $E_{n,\alpha,N,\pm}(B)$. The blue and red arrows indicate the magneto-optical CS and VPS^1 ground transitions plotted in (b). The extrapolation of the transitions to zero magnetic field yields the ground state energies $2E_{n,\alpha}(B = 0)$ of the CS and VPS. These energies are plotted vs $2l$ in (d). The solid lines represent $2E_{n,\alpha}(B = 0)$ obtained by Eq. (3), without any fit parameters.

chiral-polarized equation at $k_\parallel = 0$:

$$E^2 \chi_\alpha = \left[-\hbar^2 v_z^2 \partial_z^2 + \Delta^2(z) + \alpha \hbar v_z \partial_z \Delta(z) \right] \chi_\alpha, \quad (2)$$

where χ_α is a component of the spinor, having a well-defined chirality $\alpha = \pm 1$. Note that Eq. (2) focuses on the squared energy. In addition to the chirality, the solutions of Eq. (2) evidently depend on the potential shape $\Delta(z)$, and thus, this equation can model different relativistic spectra in condensed matter. The hereby investigated THJs display only the simplest case of a linear profile $\Delta(z)$, as shown in Figs. 2(a) and 3(a). The square energy spectrum for such linearly graded THJ, at $B = 0$ or $k_\parallel = 0$, turns out to be simply the one of a 1D quantum harmonic oscillator [17], and thus, the energy spectrum can be written as

$$E_{n,\alpha}(B = 0) = \pm \bar{\Delta} \sqrt{\frac{2\bar{\lambda}}{l} \left(n + \frac{1 + \alpha}{2} \right)}, \quad (3)$$

where the quantum number $n \geqslant 0$ is an integer, and $\alpha = \pm 1$ is the chirality of the state. Here, $\bar{\Delta} > 0$ represents the average half band gap $\bar{\Delta} = (\Delta_{NI} - \Delta_{TCI})/2$ of the THJ, which in our case is ~ 45 meV for all samples (see Table I). Likewise, $\bar{\lambda}$ is the averaged characteristic length associated with the two ends of the THJs: $\bar{\lambda} = \hbar \bar{v}_z / \bar{\Delta}$. Using the average Dirac velocity $\bar{v}_z = 4.20 \times 10^5$ m/s along the growth direction, as obtained in our previous work [14], one finds $\bar{\lambda} \sim 6$ nm. We highlight that the 1D harmonic oscillator squared energy spectrum of the THJ [Eq. (3)] directly emerges from the linear $\Delta(z)$ potential that can be therefore seen as a pseudomagnetic field with associated pseudomagnetic length written as

$\sqrt{\bar{\lambda} l}$ [49]. Consequently, the eigenfunctions χ_α are Hermite polynomials, which are shown as the squared wave functions plotted in Fig. 3(a). A resolution using the envelope function approximation is presented in Appendix C and leads to the same results. The envelope function theory, however, stands as a more general approach that can be easily applied to any arbitrary potential $\Delta(z)$.

For the ground interface state with $n = 0$ in Eq. (3), we retrieve the massless topological CS with $E_{0,-} = 0$ that displays a precisely defined chirality ($\alpha = -1$). The other solutions for $n > 0$ describe the additional twofold degenerate VPS existing in a gradual THJ, whose energies lie within the band gap of the boundary layers. Note that the lowest energy VPS

TABLE I. Energy gap and in-plane Dirac velocities of the trivial and topological thick epilayers that sandwich the gradual interface. The magneto-optical determination yields error bars of ± 5 meV on the gaps and $\pm 0.05 \times 10^5$ m/s for the velocities. The inversion parameters are fixed to $M_{NI} = 13$ eV Å^2 and $M_{TCI} = 19$ eV Å^2.

Samples	$2\Delta_{NI}$ (meV)	$2\Delta_{TCI}$ (meV)	$v_{\parallel,NI}$ ($\times 10^5$ m/s)	$v_{\parallel,TCI}$ ($\times 10^5$ m/s)
THJ-0	90	−90	5.3	4.4
THJ-50	95	−90	5.4	4.4
THJ-75	90	−90	5.3	4.4
THJ-100	95	−90	5.3	4.4
THJ-150	110	−100	5.2	4.4
THJ-200	100	−85	5.3	4.4

($n = 1$ for chirality $\alpha = -1$, and $n = 0$ for $\alpha = +1$) are bound only if $l > 2\bar{\lambda}$, i.e., only if the interface is sufficiently gradual, whereas the CS persists even for an abrupt interface, as it intrinsically results from fundamental band symmetry inversion across the interface. Note that additional details such as a possible small gap asymmetry or a slightly different band alignment and/or doping of the NI and TCI sides of the THJ are described in Ref. [50], which shows their weak influence on magneto-optical spectra.

When a magnetic field **B** is applied along the [001] direction, the Weyl and Dirac dispersions become fully quantized forming relativistic Landau levels, as sketched in Fig. 4(c), with energies given by [49]

$$E_{n,\alpha,N,\pm}(B) = \pm\sqrt{E_{n,\alpha}^2(B = 0) + 2e\hbar\bar{v}_\parallel^2 BN}. \qquad (4)$$

Here, $N = 0, 1, \ldots$ is the Landau level index and $\bar{v}_\parallel$ the averaged in-plane velocity of the trivial NI and topological TCI layers, giving $\bar{v}_\parallel \approx (v_{\parallel,\text{NI}} + v_{\parallel,\text{TCI}})/2 \sim 4.90 \times 10^5$ m/s using the values derived in Table I. Note that Eq. (4) describes pure relativistic Landau levels. The four valleys present in these compounds, located at the $\bar{X}$ points of the 2D BZ [see Fig. 1(c)], are all equivalent with respect to the [001] direction. They all verify Eq. (4) and thus contribute to the same magneto-optical absorptions.

Let us first focus on the lowest energy magneto-optical absorptions of the THJs marked in blue in Fig. 4(a). Their energetic positions are, within the experimental accuracy (1–2 meV), independent of the interface thickness. Measuring their magnetic field dependences yields the blue dots in the Landau fan charts that are presented in Fig. 4(b) for all five gradual THJs. Using Eq. (4), the blue data points are fitted by the ground interband transitions of the CS indicated by the blue arrow in Fig. 4(c), involving the Weyl state ($n = 0$ and $\alpha = -1$), giving the blue solid lines in Fig. 4(b). Evidently, these perfectly fit the experiments, giving $\bar{v}_\parallel = 5.10 \pm 0.15$ m/s independently of the THJ interface thickness. This value agrees very well with the average $\bar{v}_\parallel$ calculated from the spectra of the bulk parts of the THJ.

Interestingly, the CS is not observed in the sample THJ-0 with the sharp interface. This is attributed to the Lifshitz transition when the interface is abrupt, as seen in ARPES at a TCI-vacuum interface [see Fig. 1(b)]. Under this condition, the valley interaction between the two cones is responsible for the emergence of off-diagonal terms in the Hamiltonian given in Ref. [46] that mix the spin and orbital characters of the two cones. The overall selection rules are therefore relaxed, and the absorption is strongly weakened as compared with the single cone picture. This means that, for the abrupt THJ-0, the signature of the CS falls below the noise level of our experiments. In the case of smooth interfaces, scattering between two valleys that project at the same in-plane momentum [see Fig. 1(c)] requires a large out-of-plane momentum transfer and thus vanishes quickly when l increases [46]. For the graded THJs, the absorption coefficient of the CS is therefore proportional to the fine structure constant, like in graphene [51], and as a result, a stronger and sharper absorption is obtained.

In contrast to the observed chiral Weyl state transitions, the absorptions at higher energies, indicated by the red arrows

in Fig. 4(a), show very different behavior, as their position strongly depends on the junction thickness. This is because these transitions arise from the VPS, whose energies vary in dependence on the THJ width according to Eq. (3). Indeed, in the Landau fan charts, the experimental VPS[1] and VPS[2] absorptions, represented by the red dots in Fig. 4(b), are again in perfect agreement with the transitions calculated using Eq. (4) that are represented by the red solid lines in Fig. 4(b) and allow for the accurate determination of $2E_{n,\alpha}(B = 0)$. The corresponding ground interband transition of VPS[1] is schematically indicated by the red arrow in Fig. 4(c). We obtain an excellent fit between theory and experiments, using $\bar{v}_\parallel = 4.90 \pm 0.10$ m/s which is naturally equal to the averaged value across the heterojunction. Remarkably, even higher-order VPSs can be resolved in thick THJs, whereas they are absent for the thinner THJ-50. This result agrees with the theory because the $2l = 50$ nm junction is simply not sufficiently thick to support any higher-order VPS, the number of VPSs being $l/2\bar{\lambda}$.

As shown by Fig. 4(b), the extrapolation of the transitions to zero magnetic field yields the ground state energies $2E_{n,\alpha}(B = 0)$ of the relativistic states, as defined by Eq. (3). The resulting values, which correspond to the gap between the hole and electronlike CS and VPS[n], are plotted in Fig. 4(d) as a function of the THJ interface width, evidencing the anticipated decrease of the VPS energy with increasing junction width as well as the constant zero-gap energy for the CS. The theoretical predictions depicted by Eq. (3) are represented by the solid lines in Fig. 4(d), giving striking evidence for the perfect agreement between theory and experiments for the whole series of THJs without adjustable parameters. Our experiments impressively demonstrate the $E_{n,\alpha} \sim \sqrt{n/l}$ dependence of the VPS, which validates quantitatively the VP [7] and Lu and Goerbig [17] theories even with remarkable accuracy. Moreover, we experimentally demonstrate a fundamental property of topology, namely, the immutable presence of the CS if a band crossing occurs. Last but not least, it is noted that relativistic CS and VPS transitions are not observed when the magnetic field is in the layer plane of the THJ (see Fig. 5), which confirms the 2D character of the interface CS and VPS [49].

IV. DISCUSSION

As described above, VPSs only appear in smooth THJs in which the band gap profile $\Delta(z)$ varies slowly over a wide length scale $l > 2\bar{\lambda}$. Thus, they do not exist when the THJ is abrupt. However, other types of massive 2D states can appear in abrupt THJs, originating from different mechanisms. For instance, they can be induced when an abrupt THJ is subjected to a large electrostatic band-bending potential superimposed over an abrupt gap change at the interface, as has been shown, e.g., by ARPES for TI surfaces such as Bi_2Se_3 where, by surface doping induced by molecular gas adsorption or alkaline element deposition [52–54], a triangular potential well is formed by the resulting band bending at the surface, leading to the appearance electrostatically confined states (ECSs). A similar effect can also be induced by applying a bias voltage across an abrupt THJ [55]. Most importantly, an applied electric field cannot induce a gradual $\Delta(z)$ band inversion as
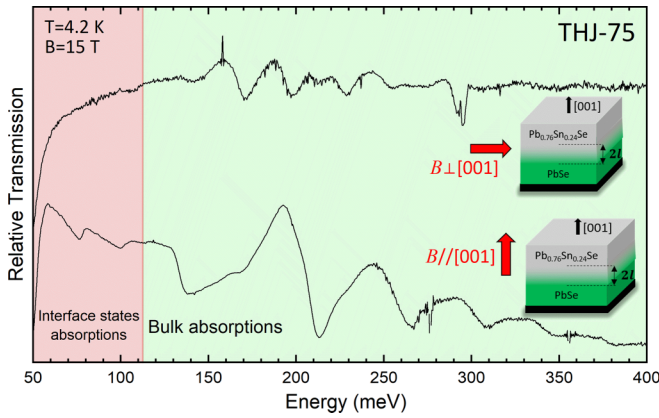
FIG. 5. Spectra of THJ-75 at $T = 4.2$ K and $B = 15$ T for two different geometries. Upper spectrum: **B** is in the plane of the sample. Lower spectrum: Faraday geometry (**B** perpendicular to the sample, i.e., parallel to [001]). The high- and low-energy parts are shaded in distinct colors.

required for the VPS, and for these reasons, the VPSs do not need any external perturbation to appear in a gradual THJ. It is noted that the strong electrostatic potential required to form ECSs will induce a strong Rashba splitting which drastically affects the ECS dispersions.

Here, 2D massive states can also naturally emerge at abrupt THJs made from Kane materials, like in HgTe/HgCdTe heterointerfaces [56–58]. In this case, the presence of the heavy hole band is responsible for an intricate electronic density at the surface [59–61]. The topological interface state, whose presence is driven by the Γ_6-Γ_8^l inverted band gap, shows a dispersion that is strongly hybridized with heavy hole states (Γ_8^h) and thus does not display a Weyl-like dispersion like the CS in VP-THJs observed in this paper [57,60]. Moreover, the topological interface state in Kane materials resides in the Γ_6-Γ_8^l inverted gap and thus is buried far below the Γ_8^h band. An electrostatic potential is then needed to shift the CS into the experimentally reachable Γ_8^h-Γ_8^l gap (slightly opened by a tensile strain) [55–57]. The additional massive states that such an abrupt interface can host are known as the Dyakonov-Khaetskii states (DKSs) [59]. They are solutions to the Luttinger Hamiltonian, which depicts the Γ_8^h-Γ_8^l subspace only, thus, their dispersions are parabolic and not Dirac-like [60].

The responses of the ECSs and DKSs toward an applied electrostatic field are different [50,58]; whereas VPSs are only shifted upward or downward in energy (depending on the sign of the field) and even disappear above a certain critical field [50], ECSs and DKSs are observable only under a sufficiently high electric field [57]. The nature of the VPS confinement is therefore fundamentally different from the ECS and/or DKS. This also follows from the fact that, while the ESC and DKS are essentially confined to only one side of the THJ, i.e., their wave functions are localized in a region of constant band topology, those of the VPS nearly equally extend over both TI and NI regions, as shown by Fig. 3.

Last but not least, the ECS and DKS do not display the characteristic electron-hole symmetry of the VPS; for an upward or downward band bending, the ESCs are formed only

either in the valence or in the conduction band; and the parabolic DKSs are highly asymmetric by nature and form only electronlike states at the HgTe/HgCdTe interface, for instance [60]. Indeed, only THJs made of 3D Dirac materials such as PbSn(Se,Te) are described by a Hamiltonian in a supersymmetric form [8] which leads to a pure relativistic spectrum of electron-hole symmetric Weyl and Dirac states, as demonstrated in this paper. For all these reasons, the ECS and DKS are not to be confused with the VPSs that are of fundamentally different origin.

V. CONCLUSIONS

In conclusion, we have shown that the smooth interconnection of materials with different band topologies exposes a rich relativistic spectrum of coexisting 2D chiral Weyl and massive Dirac VP states that are both confined to the same interface. The VPSs emerge only for a sufficiently smooth THJ, and they expose an energy spectrum that is controlled on demand by the interface width. Using magnetospectroscopy of engineered NI/TCI heterojunctions based on the perfect Dirac PbSe/Pb$_{1-x}$Sn$_x$Se system, we demonstrated the tunability of the energy spectrum with Dirac VPSs quantized in terms of $\sqrt{n/l}$ as well as their coexistence with the zero-energy massless Weyl fermions that persist for arbitrary interfaces. In this paper, we thus offer an unequivocally experimental validation of the VP theory. We also highlight the different nature of the gapless CS at a gradual topological interface where its Gaussian envelope function strongly differs from that of the cusped shape at abrupt interfaces.

The demonstrated basic principle of topological band profile engineering of THJs can be generalized and applied to other topological systems such as (Bi$_{1-x}$In$_x$)$_2$Se$_3$ or BiTl(S$_{1-\delta}$Se$_\delta$)$_2$ or the potential topological superconductor Sn$_{1-x}$In$_x$Te [62,63], where similar smooth topological transitions can be realized by grading of composition [64,65]. Engineering of the topological interface profiles thus opens the door for further exploration of other nonlinear gap variations that could simulate different relativistic particles and/or effects. By establishing a textbook platform to access Weyl and Dirac fermions, our work paves the way for the investigation of various symmetry-breaking effects on multiple relativistic particles by introducing magnetism or ferroelectric polarization that can be induced in the IV-VI TCIs, e.g., by Mn or Ge doping [1,33,66,67]. Last but not least, VPSs have been theoretically predicted to be encountered in various other scenarios such as in graphene nanoribbons [68], partial dislocations in bilayer graphene [69], as well as topological superconductor–superconductor heterojunctions, so that VPSs can emerge alongside Majorana fermions [70].

APPENDIX A: THJ GROWTH

The IV-VI-based THJs were grown by MBE on (001) KCl substrates. Layers with incrementally varying $Pb_{1-x}Sn_xSe$ compositions were grown on top of each other using PbSe and SnSe effusion sources. The Sn content in each layer was controlled by adjusting the SnSe : PbSe beam flux ratio that was measured accurately by the quartz microbalance method. The carrier concentration in the THJs was controlled using a Bi_2Se_3 source to induce a slightly *n*-doping of the $Pb_{1-x}Sn_xSe$ layers in the THJ and compensate the native *p*-type character of the material that increases with increasing Sn content. Growth was carried out at substrate temperatures ~ 300 °C and ultrahigh vacuum conditions ($<5 \times 10^{-10}$ mbar). Here, 2D growth was sustained throughout the whole growth process, as checked by *in situ* high-energy electron diffraction.

To deliberately form a slowly varying Sn gradient across the THJs, the graded junction region was split up in nine successive subregions, each consisting of an ultrashort-period SL consisting of PbSe and $Pb_{0.76}Sn_{0.24}Se$ layers with varying thickness ratios, as shown schematically in the Fig. 6. The period of these SLs was fixed to ~ 2.5 nm, and the total thickness of each SL stack was $\sim 10\%$ of the designated entire junction width. The increment in the average Sn content in successive SLs was therefore 2.4%, but these incremental steps were further smoothed by Sn/Pb interdiffusion. For the thicker THJ-150 and THJ-200, the steps in the Sn increments were reduced to 2 and 1.5%, respectively.

The NI PbSe and TCI $Pb_{0.76}Sn_{0.24}Se$ reference layers used for ARPES experiments were grown under the same conditions and consist of 400-nm-thick epilayers. However, they were higher *n*-doped to ensure a Fermi energy sufficiently high in the conduction band to observe the conduction band in the ARPES measurements.

APPENDIX B: MAGNETO-OPTICAL CHARACTERIZATION OF THE THJs

Magneto-optical measurements in Faraday geometry were performed on the six investigated THJ samples of this paper. Figure 7 shows the magneto-optical results obtained on sample THJ-100, which stand for a typical result for the six investigated THJs in the main text. The transmission spectra plotted in Fig. 7(a) show several absorption lines that shift to higher energies when the magnetic field is increased, revealing optical transitions between Landau levels. The absorption energies, marked by colored arrows, are extracted, and their variations vs magnetic field are represented by the colored dots in Fig. 7(b). A fit of the high-energy part (>100 meV) is achieved by using the expression of massive Dirac-Landau levels corresponding to those of 3D $Pb_{1-x}Sn_xSe$ alloys [14,40,71]:

$$E_{N,\pm,\xi} = \frac{2\xi M_{TCI/NI}eB}{\hbar}$$
$$\pm \sqrt{\left(\Delta_{TCI/NI} + \frac{2M_{TCI/NI}eBN}{\hbar}\right)^2 + 2e\hbar v_{\parallel,TCI/NI}^2 BN},$$
(B1)

where $N \geqslant 0$ is the Landau level index, and $\xi = \pm 1$ denotes the two spin orientations. The inversion parameter $M_{TCI/NI}$ accounts for the effect of all other remote bands, which is rather small as far bands are typically 2 eV above and below the Dirac point [15]. Here, $\Delta_{TCI/NI}$, $v_{\parallel,TCI/NI}$, and $M_{TCI/NI}$ are fitting parameters which depend on the chemical composition and temperature of the $Pb_{1-x}Sn_xSe$ alloy [14,71].

The solid lines in Fig. 7(b) represent the calculated transition energies, using the parameters given in Table I, occurring between Landau levels in Faraday geometry for $B//[001]$: $|E_{N\pm1,+} - E_{N,-}|$ at fixed ξ. The fits of the experimental data (green and black dots) involve two Landau level spectra, both described by Eq. (B1). They correspond to the two thick epilayers that sandwich the gradual interface: PbSe and $Pb_{0.76}Sn_{0.24}Se$. The fits lead to the three band parameters for each layer: $2\Delta_{TCI/NI}$ is extracted by the experimental extrapolation of the absorptions at $B = 0$, and $v_{\parallel,TCI/NI}$ and $M_{TCI/NI}$ account for the slope of the transitions vs B. The
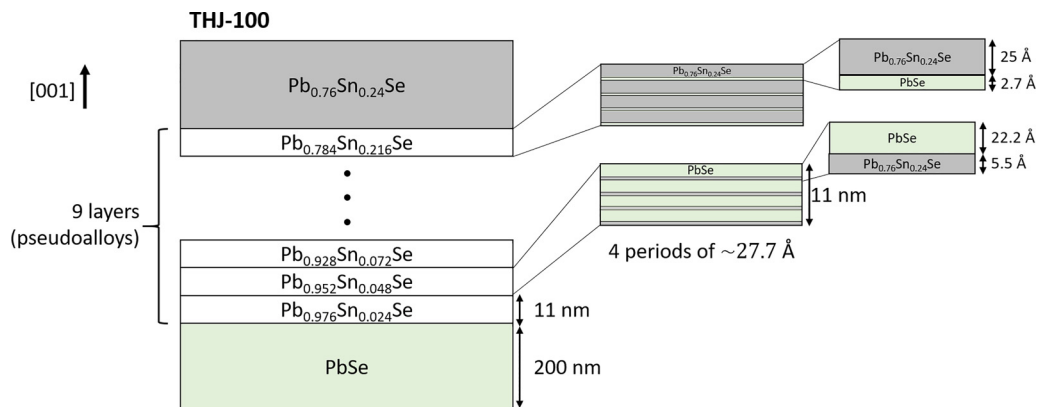

FIG. 6. Scheme of the topological heterojunction (THJ) growth, with the deliberate formation of the gradual interface. The values shown here correspond to THJ-100. Similar values were used for the other THJs.
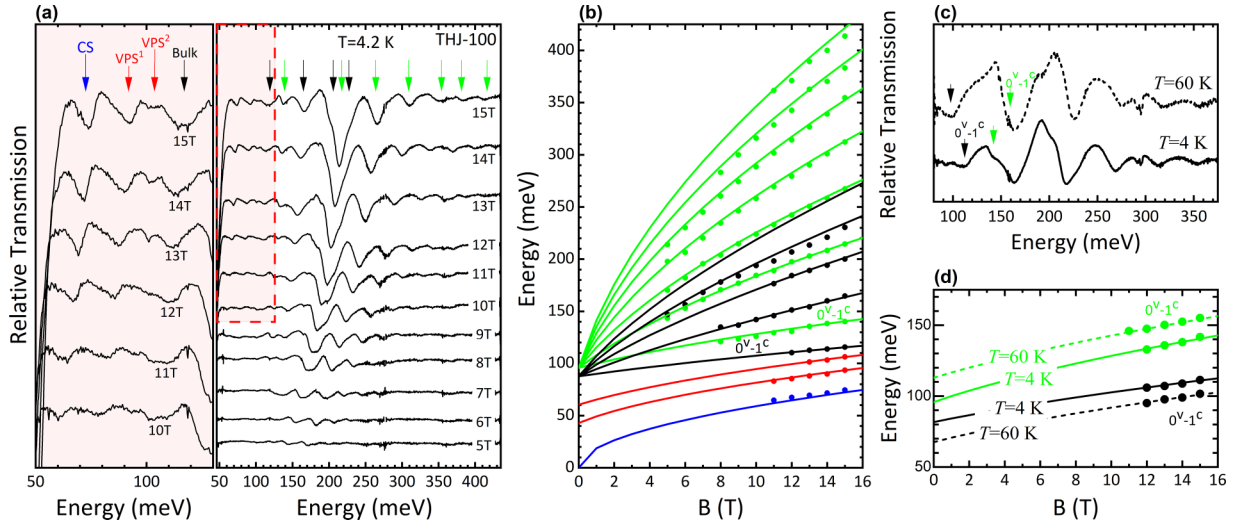
FIG. 7. (a) Normalized magneto-optical transmission spectra of THJ-100 at $T = 4.2$ K and for different magnetic fields. The colored arrows indicate the observed absorptions at $B = 15$ T. Left: Zoom of the low energy part at high magnetic field, corresponding to the area shown inside the dashed red line on the right panel. (b) Full magneto-optical fan chart of THJ-100, where the absorption energies vs magnetic field are represented by dots. The solid lines are the calculated transitions between Landau levels using Eq. (B1). In green and black, the absorptions and transitions are attributed to PbSe and $Pb_{0.76}Sn_{0.24}Se$, respectively. (c) Spectra at $B = 15$ T at $T = 4.2$ K (solid line) and $T = 60$ K (dashed line). (d) Fit of the ground transitions 0^v-1^c [or $|E_{1,+} - E_{0,-}|$ following Eq. (B1)] attributed to the two thick epilayers at $T = 4.2$ K (solid lines) and $T = 60$ K (dashed lines).

band parameters giving the best fits are listed in Table I. The black series presents the smallest velocity value $v_{\parallel,\text{TCI}}$ (slowly dispersive transitions) and is thus associated with $Pb_{0.76}Sn_{0.24}Se$, whose high Sn content is responsible for its topological character [23,32]. In this sample, the trivial PbSe layer (green series) has a gap of $+95$ meV, and the one of the topological $Pb_{0.76}Sn_{0.24}Se$ layer is $2\Delta_{\text{TCI}} = -90$ meV.

To confirm the trivial and topological character of each layer, temperature-dependent measurements on the same THJ sample are performed. The spectra at $B = 15$ T from $T = 4.2$ to 60 K [see Fig. 7(c)] show a shift of the absorptions toward high energies for the green series and toward low energies for the black series. As shown by the corresponding fits presented in Fig. 7(d), this effect is due to an increase of the absolute gap value for PbSe, while it is decreasing for $Pb_{0.76}Sn_{0.24}Se$ (see the extrapolations at $B = 0$). This temperature dependence of the absolute energy gap is direct evidence of the inverted band structure of $Pb_{0.76}Sn_{0.24}Se$ [21,72]. Therefore, this system realizes a heterojunction with two topologically different epilayers having gaps of nearly similar absolute values but with opposite signs. These data corroborate and support the ARPES measurements exposed in the main text.

APPENDIX C: k · p MODELING OF A THJ

Beyond the analytical formula Eq. (3), numerical **k · p** calculations in the envelope function approximation have been performed to unravel the relativistic spectrum of a THJ. Using Hamiltonians developed in Refs. [40–42,73], and substituting $k_z \rightarrow -i\hbar \frac{\partial}{\partial z}$ to account for the confinement, we have

$$\begin{bmatrix} -\Delta(z) - E & \xi i\hbar v_z \frac{\partial}{\partial z} \\ \xi i\hbar v_z \frac{\partial}{\partial z} & \Delta(z) - E \end{bmatrix} \begin{bmatrix} F_1^{(j)} \\ \xi F_2^{(j)} \end{bmatrix} = 0, \qquad \text{(C1)}$$

where $\xi = \pm 1$ denotes again the Kramers pairs. The system in Eq. (C1) evolves in

$$-[\Delta(z) + E_j]F_1^{(j)} + \hbar^2 v_z^2 \frac{d}{dz} \frac{1}{\Delta(z) - E_j} \frac{dF_1^{(j)}}{dz} = 0$$

$$F_2^{(j)} = -\frac{i\hbar v_z}{(\Delta(z) - E_j)} \frac{dF_1^{(j)}}{dz}.$$

Let us solve this problem for an abrupt $\Delta(z)$ potential. If it is so, one can write $F_1^{(j)}$ as a sum of an incoming and outgoing wave on both sides of the abrupt $\Delta(z)$ variation. These waves can be evanescent or propagative depending on the sign of $\Delta(z) - E_j$. Then at the abrupt interface, the solutions found on both sides are matched so that $F_1^{(j)}$ and $\frac{1}{\Delta(z)-E_j} \frac{dF_1^{(j)}}{dz}$ are continuous.

To model a THJ, the smooth interface can be divided into $N + 1$ parts, where Δ_p is independent from z with $0 \leqslant p \leqslant N$ and N the number of abrupt interfaces. The smooth gradual potential is thus modeled by a succession of N abrupt interfaces separating regions of constant gaps Δ_p. When N tends to infinity, we retrieve a smooth potential. Usually, $N = 100$ ensures a good convergence of the numerical computation. On one step of the staircase profile, the solutions are known (see above), and one can write the spinor wave function as a sum of incoming and outgoing waves:

$$\varphi_p(z) = A_p \begin{pmatrix} \frac{\hbar v_z k_p}{\Delta_p + E} \\ 1 \end{pmatrix} \exp(ik_p z) + B_p \begin{pmatrix} -\frac{\hbar v_z k_p}{\Delta_p + E} \\ 1 \end{pmatrix} \exp(-ik_p z),$$
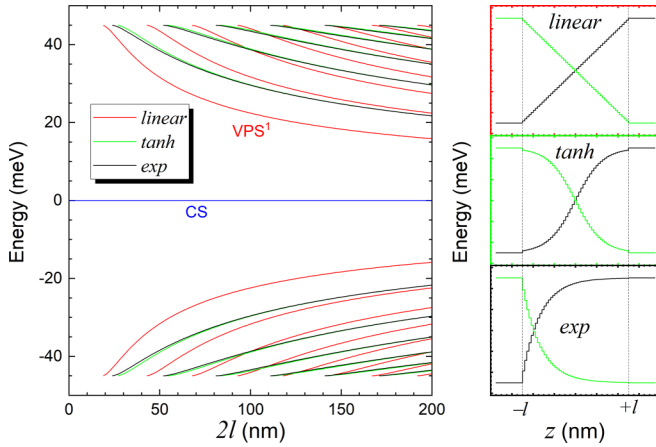
FIG. 8. Calculated chiral state (CS) and Volkov-Pankratov state (VPS) energies vs interface thickness $2l$, with the parameters listed in Table I and with different potential profile: linear (red), hyperbolic tangent (green) and exponential (black).

with the wave vector:

$$k_p = \begin{cases} \frac{1}{\hbar v_z}\sqrt{E^2 - \Delta_p^2}, & |E| > |\Delta_p| \\ \frac{i}{\hbar v_z}\sqrt{\Delta_p^2 - E^2}, & |E| < |\Delta_p|. \end{cases}$$

Here, A_p and B_p are constants that are determined by using the continuity conditions at the N interfaces. When the wave function is imposed to vanish far from the global gradual interface, i.e., in the PbSe and $Pb_{0.76}Sn_{0.24}Se$ thick epilayers, only a few solutions remain at energies corresponding to VPSs and CSs. The wave function is then normalized.

The major advantage of this resolution is that the staircase function Δ_p is obtained by taking the targeted $\Delta(z)$ potential and substituting z by $l(\frac{2p}{N} - 1)$. It is therefore easy to consider other nonlinear potential profiles. Figure 8 shows examples of different relativistic VP energy spectra, obtained with three distinct potential profiles: linear, hyperbolic tangent, and exponential.

APPENDIX D: THJ MAGNETOSPECTROSCOPY WITH IN-PLANE MAGNETIC FIELD

We performed a magneto-optical experiment where the sample THJ-75 was placed parallel to the magnetic field direction, i.e., **B** is in the (001) plane. The spectra at $B = 15$ T is shown in Fig. 5. Whereas the high-energy part ($2\Delta_{TCI,NI} \gtrsim 100$ meV), which hosts the absorptions minima due to 200-nm-thick epilayers PbSe and $Pb_{0.76}Sn_{0.24}Se$, still exhibits inter-Landau-level absorptions, the low-energy part (highlighted in red) shows no absorption minima. This behavior is expected for 2D states when the magnetic field is applied perpendicularly to the confinement direction. Indeed, no Landau quantization occurs in this geometry, i.e., the dispersions remain conical, and thus, no transitions between Landau levels appear. Moreover, the density of states is not increased for higher magnetic fields, as is the case with a Landau quantization, where each level displays a eB/h degeneracy. Therefore, the Fermi level remains above the CS and VPS, as they are located within the gap of the THJ two ends PbSe and $Pb_{0.76}Sn_{0.24}Se$, as they are located within the gap of the THJ two ends PbSe and $Pb_{0.76}Sn_{0.24}Se$. As a result, no transitions between states located at the band edges are allowed due to a population effect. If the Fermi levels of the investigated THJs were lower, the absorptions between VPSs or CSs would have the shape of their densities of state; thus, we would expect a step (for the VPS) and/or a line (for the CS) in the transmission spectra [49]. This is not observed here.

[1] N. P. Armitage, E. J. Mele, and A. Vishwanath, Weyl and Dirac semimetals in three-dimensional solids, Rev. Mod. Phys. **90**, 015001 (2018).

[2] G. W. Semenoff, Condensed-Matter Simulation of a Three-Dimensional Anomaly, Phys. Rev. Lett. **53**, 2449 (1984).

[3] M. Z. Hasan, S.-Y. Xu, and G. Bian, Topological insulators, topological superconductors and Weyl Fermion semimetals: Discoveries, perspectives and outlooks, Phys. Scr. **2015**, 14001 (2015).

[4] M. Z. Hasan and C. L. Kane, Colloquium: Topological insulators, Rev. Mod. Phys. **82**, 3045 (2010).

[5] X. L. Qi and S. C. Zhang, Topological insulators and superconductors, Rev. Mod. Phys. **83**, 1057 (2011).

[6] Y. Ando and L. Fu, Topological crystalline insulators and topological superconductors: From concepts to materials, Annu. Rev. Condens. Matter Phys. **6**, 361 (2015).

[7] B. Volkov and O. Pankratov, Two-dimensional massless electrons in an inverted contact, JETP Lett. **42**, 178 (1985).

[8] O. A. Pankratov, S. V Pakhomov, and B. A. Volkov, Supersymmetry in heterojunctions: Band-inverting contact on the basis of $Pb_{1-x}Sn_xTe$ and $Hg_{1-x}Cd_xTe$, Solid State Commun. **61**, 93 (1987).

[9] B. A. Bernevig, T. L. Hughes, and S. Zhang, Quantum spin Hall effect and topological phase transition in HgTe quantum wells, Science **314**, 1757 (2006).

[10] M. König, S. Wiedmann, C. Brüne, A. Roth, H. Buhmann, L. W. Molenkamp, X.-L. Qi, and S.-C. Zhang, Quantum spin Hall insulator state in HgTe quantum wells, Science **318**, 766 (2007).

[11] C.-X. Liu, S.-C. Zhang, and X.-L. Qi, The quantum anomalous Hall effect: Theory and experiment, Annu. Rev. Condens. Matter Phys. **7**, 301 (2016).

[12] C.-Z. Chang, J. Zhang, X. Feng, J. Shen, Z. Zhang, M. Guo, K. Li, Y. Ou, P. Wei, L.-L. Wang *et al.*, Experimental observation of the quantum anomalous Hall effect in a magnetic topological insulator, Science **340**, 167 (2013).

[13] O. A. Pankratov, Understanding surface states of topological insulators, Phys.-Uspekhi **61**, 1116 (2018).

[14] G. Krizman, B. A. Assaf, T. Phuphachong, G. Bauer, G. Springholz, L. A. de Vaulchier, and Y. Guldner, Dirac parameters and topological phase diagram of $Pb_{1-x}Sn_xSe$ from magnetospectroscopy, Phys. Rev. B **98**, 245202 (2018).

[15] G. Martinez, Band inversion in $Pb_{1-x}Sn_xSe$ alloys under hydrostatic pressure. II. Galvanomagnetic properties, Phys. Rev. B **8**, 4686 (1973).

[16] B. M. Wojek, P. Dziawa, B. J. Kowalski, A. Szczerbakow, A. M. Black-Schaffer, M. H. Berntsen, T. Balasubramanian, T. Story, and O. Tjernberg, Band inversion and the topological phase transition in (Pb,Sn)Se, Phys. Rev. B **90**, 161202(R) (2014).

[17] X. Lu and M. O. Goerbig, Dirac quantum well engineering on the surface of a topological insulator, Phys. Rev. B **102**, 155311 (2020).

[18] L. Fu, Topological Crystalline Insulators, Phys. Rev. Lett. **106**, 106802 (2011).

[19] T. H. Hsieh, H. Lin, J. Liu, W. Duan, A. Bansil, and L. Fu, Topological crystalline insulators in the SnTe material class, Nat. Commun. **3**, 982 (2012).

[20] P. Dziawa, B. J. Kowalski, K. Dybko, R. Buczko, A. Szczerbakow, M. Szot, E. Łusakowska, T. Balasubramanian, B. M. Wojek, M. H. Berntsen *et al.*, Topological crystalline insulator states in $Pb_{1-x}Sn_xSe$, Nat. Mater. **11**, 1023 (2012).

[21] Z.-Y. Ye, H.-X. Deng, H.-Z. Wu, S.-S. Li, S.-H. Wei, and J.-W. Luo, The origin of electronic band structure anomaly in topological crystalline insulator group-IV tellurides, Npj Comput. Mater. **1**, 15001 (2015).

[22] R.-J. Slager, A. Mesaros, V. Juričić, and J. Zaanen, The space group classification of topological band-insulators, Nat. Phys. **9**, 98 (2013).

[23] G. Bauer, M. Kriechbaum, Z. Shi, and M. Tacke, IV–VI quantum wells for infrared lasers, J. Nonlinear Opt. Phys. Mater. **04**, 283 (1995).

[24] Z. Shi, M. Tacke, A. Lambrecht, and H. Böttner, Midinfrared lead salt multi-quantum-well diode lasers with 282 K operation, Appl. Phys. Lett. **66**, 2537 (1995).

[25] G. Springholz, Molecular beam epitaxy of IV-VI semiconductors: Fundamentals, low dimensional structures, and device applications, in *Molecular Beam Epitaxy: From Research to Mass Production*, 2nd ed. (Elsevier Science Publishing Co., Amsterdam, 2018), Chap. 11, pp. 211–276.

[26] M. Eibelhuber, T. Schwarzl, S. Pichler, W. Heiss, and G. Springholz, Near room temperature continuous-wave laser operation from type-I interband transitions at wavelengths beyond 4 μm, Appl. Phys. Lett. **97**, 61103 (2010).

[27] I. Kang and F. W. Wise, Electronic structure and optical properties of PbS and PbSe quantum dots, J. Opt. Soc. Am. B **14**, 1632 (1997).

[28] G. Springholz, T. Schwarzl, W. Heiss, G. Bauer, M. Aigle, H. Pascher, and I. Vavra, Midinfrared surface-emitting PbSe/PbEuTe quantum-dot lasers, Appl. Phys. Lett. **79**, 1225 (2001).

[29] A. Katzir, R. Rosman, Y. Shani, K. H. Bachem, H. Böttner, and H. Preier, Tunable lead salt lasers, in *Handbook of Solid State Lasers*, edited by P. K. Cheo (Marcel Dekker, New York, 1989), pp. 227–347.

[30] A. R. Calawa, J. O. Dimmock, T. C. Harman, and I. Melngailis, Magnetic Field Dependence of Laser Emission in $Pb_{1-x}Sn_xSe$ Diodes, Phys. Rev. Lett. **23**, 7 (1969).

[31] G. Springholz, T. Schwarzl, and W. Heiss, Mid-infrared vertical cavity surface emitting lasers based on the lead salt compounds BT, in *Mid-Infrared Semiconductor Optoelectronics*, edited by A. Krier (Springer, London, 2006), pp. 265–301.

[32] B. A. Assaf, T. Phuphachong, V. V Volobuev, G. Bauer, G. Springholz, L.-A. De Vaulchier, and Y. Guldner, Magnetooptical determination of a topological index, npj Quantum Mater. **2**, 26 (2017).

[33] A. Lau and C. Ortix, Topological Semimetals in the SnTe Material Class: Nodal Lines and Weyl Points, Phys. Rev. Lett. **122**, 186801 (2019).

[34] L. Tian, K. Satya, K. Jinwoong, G. Quinn, L. Jingjing, K. Nicholas, R. J. Cava, and N. P. Ong, A pressure-induced topological phase with large Berry curvature in $Pb_{1-x}Sn_xTe$, Sci. Adv. **3**, e1602510 (2021).

[35] J. Liu, C. Fang, and L. Fu, Tunable Weyl fermions and fermi arcs in magnetized topological crystalline insulators, Chin. Phys. B **28**, 47301 (2019).

[36] P. Sessi, D. Di Sante, A. Szczerbakow, F. Gott, S. Wilfert, H. Schmidt, T. Bathon, P. Dziawa, M. Greiter, T. Neupert *et al.*, Robust spin-polarized midgap states at step edges of topological crystalline insulators, Science **354**, 1269 (2016).

[37] D. Iaia, C.-Y. Wang, Y. Maximenko, D. Walkup, R. Sankar, F. Chou, Y.-M. Lu, and V. Madhavan, Topological nature of step-edge states on the surface of the topological crystalline insulator $Pb_{0.7}Sn_{0.3}Se$, Phys. Rev. B **99**, 155116 (2019).

[38] J. Liu and L. Fu, Electrically tunable quantum spin Hall state in topological crystalline insulator thin films, Phys. Rev. B **91**, 081407(R) (2015).

[39] S. Safaei, M. Galicka, P. Kacman, and R. Buczko, Quantum spin Hall effect in IV-VI topological crystalline insulators, New J. Phys. **17**, 063041 (2015).

[40] D. L. Mitchell and R. F. Wallis, Theoretical energy-band parameters for the lead salts, Phys. Rev. **151**, 581 (1966).

[41] J. O. Dimmock and G. B. Wright, Band edge structure of PbS, PbSe, and PbTe, Phys. Rev. **135**, A821 (1964).

[42] H. Pascher, G. Bauer, and R. Grisar, Magnetooptical investigations and four-wave-mixing spectroscopy of PbSe, Phys. Rev. B **38**, 3383 (1988).

[43] A. J. Strauss, Inversion of conduction and valence bands in $Pb_{1-x}Sn_xSe$ alloys, Phys. Rev. **157**, 608 (1967).

[44] B. M. Wojek, M. H. Berntsen, V. Jonsson, A. Szczerbakow, P. Dziawa, B. J. Kowalski, T. Story, and O. Tjernberg, Direct observation and temperature control of the surface Dirac gap in a topological crystalline insulator, Nat. Commun. **6**, 8463 (2015).

[45] P. Barone, T. Rauch, D. Di Sante, J. Henk, I. Mertig, and S. Picozzi, Pressure-induced topological phase transitions in rocksalt chalcogenides, Phys. Rev. B **88**, 045207 (2013).

[46] J. Liu, W. Duan, and L. Fu, Two types of surface states in topological crystalline insulators, Phys. Rev. B **88**, 241303(R) (2013).

[47] G. Bauer, Magnetooptical properties of IV–VI compounds, in *Narrow Gap Semiconductors Physics and Applications*, edited by W. Zawadzki, Lecture Notes in Physics, Vol. 133 (Springer, Berlin, Heidelberg, 1980), pp. 427–446.

[48] R. Jakieła, M. Galicka, P. Dziawa, G. Springholz, and A. Barcz, SIMS accurate determination of matrix composition of topological crystalline insulator material $Pb_{1-x}Sn_xSe$, Surf. Interface Anal. **52**, 71 (2020).

[49] X. Lu and M. O. Goerbig, Magneto-optical signatures of Volkov-Pankratov states in topological insulators, Europhys. Lett. **126**, 67004 (2019).

[50] S. Tchoumakov, V. Jouffrey, A. Inhofer, E. Bocquillon, B. Plaçais, D. Carpentier, and M. O. Goerbig, Volkov-Pankratov states in topological heterojunctions, Phys. Rev. B **96**, 201302(R) (2017).

[51] A. K. Geim and K. S. Novoselov, The rise of graphene, Nat. Mater. **6**, 183 (2007).

[52] M. Bianchi, D. Guan, S. Bao, J. Mi, B. B. Iversen, P. D. C. King, and P. Hofmann, Coexistence of the topological state and a two-dimensional electron gas on the surface of Bi_2Se_3, Nat. Commun. **1**, 128 (2010).

[53] M. S. Bahramy, P. D. C. King, A. de la Torre, J. Chang, M. Shi, L. Patthey, G. Balakrishnan, P. Hofmann, R. Arita, N. Nagaosa *et al.*, Emergent quantum confinement at topological insulator surfaces, Nat. Commun. **3**, 1159 (2012).

[54] Z.-H. Zhu, G. Levy, B. Ludbrook, C. N. Veenstra, J. A. Rosen, R. Comin, D. Wong, P. Dosanjh, A. Ubaldini, P. Syers *et al.*, Rashba Spin-Splitting Control at the Surface of the Topological Insulator Bi_2Se_3, Phys. Rev. Lett. **107**, 186405 (2011).

[55] T. L. van den Berg, M. R. Calvo, and D. Bercioux, Living on the edge: Topology, electrostatics, and disorder, Phys. Rev. Res. **2**, 013171 (2020).

[56] D. M. Mahler, J.-B. Mayer, P. Leubner, L. Lunczer, D. Di Sante, G. Sangiovanni, R. Thomale, E. M. Hankiewicz, H. Buhmann, C. Gould *et al.*, Interplay of Dirac Nodes and Volkov-Pankratov Surface States in Compressively Strained HgTe, Phys. Rev. X **9**, 031034 (2019).

[57] D. M. Mahler, V. L. Müller, C. Thienel, J. Wiedenmann, W. Beugeling, H. Buhmann, and L. W. Molenkamp, Massive and topological surface states in tensile-strained HgTe, Nano Lett. **21**, 9869 (2021).

[58] A. Inhofer, S. Tchoumakov, B. A. Assaf, G. Fève, J. M. Berroir, V. Jouffrey, D. Carpentier, M. O. Goerbig, B. Plaçais, K. Bendias *et al.*, Observation of Volkov-Pankratov states in topological HgTe heterojunctions using high-frequency compressibility, Phys. Rev. B **96**, 195104 (2017).

[59] M. I. D'yakonov and A. V. Khaetskii, Surface states in gapless semiconductors, JETP Lett. **33**, 110 (1981).

[60] S. S. Krishtopenko, M. Antezza, and F. Teppe, Hybridization of topological surface states with a flat band, J. Phys. Condens. Matter **32**, 165501 (2020).

[61] O. V. Kibis, O. Kyriienko, and I. A. Shelykh, Structure of surface electronic states in strained mercury telluride, New J. Phys. **21**, 43016 (2019).

[62] J. Wang, W. Powers, Z. Zhang, M. Smith, B. J. McIntosh, S. K. Bac, L. Riney, M. Zhukovskyi, T. Orlova, L. P. Rokhinson *et al.*, Observation of coexisting weak localization and superconducting fluctuations in strained $Sn_{1-x}In_xTe$ thin films, Nano Lett. **22**, 792 (2022).

[63] G. Balakrishnan, L. Bawden, S. Cavendish, and M. R. Lees, Superconducting properties of the In-substituted topological crystalline insulator SnTe, Phys. Rev. B **87**, 140507(R) (2013).

[64] S.-Y. Xu, Y. Xia, L. A. Wray, S. Jia, F. Meier, J. H. Dil, J. Osterwalder, B. Slomski, A. Bansil, H. Lin *et al.*, Topological phase transition and texture inversion in a tunable topological insulator, Science **332**, 560 (2011).

[65] M. Brahlek, N. Bansal, N. Koirala, S.-Y. Xu, M. Neupane, C. Liu, M. Z. Hasan, and S. Oh, Topological-Metal to Band-Insulator Transition in $(Bi_{1-x}In_x)_2Se_3$ Thin Films, Phys. Rev. Lett. **109**, 186403 (2012).

[66] G. Bauer, H. Pascher, and W. Zawadzki, Magneto-Optical properties of semimagnetic lead chalcogenides, Semicond. Sci. Technol. **7**, 703 (1992).

[67] E. Bangert, G. Bauer, E. J. Fantner, and H. Pascher, Magneto-optical investigations of phase-transition-induced band-structure changes of $Pb_{1-x}Ge_xTe$, Phys. Rev. B **31**, 7958 (1985).

[68] T. L. van den Berg, A. De Martino, M. R. Calvo, and D. Bercioux, Volkov-Pankratov states in topological graphene nanoribbons, Phys. Rev. Res. **2**, 023373 (2020).

[69] S. Theil, R. Gupta, F. Wullschläger, B. Meyer, S. Sharma, and S. Shallcross, Volkov-Pankratov states in a 2*d* material: Excited states of a structural soliton, arXiv:2203.16079.

[70] D. J. Alspaugh, D. E. Sheehy, M. O. Goerbig, and P. Simon, Volkov-Pankratov states in topological superconductors, Phys. Rev. Res. **2**, 023146 (2020).

[71] K. K. Tikuišis, J. Wyzula, L. Ohnoutek, P. Cejpek, K. Uhlířová, M. Hakl, C. Faugeras, K. Výborný, A. Ishida, M. Veis *et al.*, Landau level spectroscopy of the PbSnSe topological crystalline insulator, Phys. Rev. B **103**, 155304 (2021).

[72] G. Krizman, B. A. Assaf, G. Bauer, G. Springholz, L. A. de Vaulchier, and Y. Guldner, Miniband engineering and topological phase transitions in topological-insulator—normal-insulator superlattices, Phys. Rev. B **103**, 235302 (2021).

[73] M. S. Adler, C. R. Hewes, and S. D. Senturia, $\tilde{k} \cdot \tilde{p}$ model for the magnetic energy levels in PbTe and $Pb_{1-x}Sn_xTe$, Phys. Rev. B **7**, 5186 (1973).